Interfacial self-healing polymer electrolytes for ultralong-life solid-state lithium-sulfur batteries

Fei Pei
Huazhong University of Science and Technology
Lin Wu
Huazhong University of Science and Technology
Yi Zhang
Huazhong University of Science and Technology
Yaqi Liao
Huazhong University of Science and Technology
Qi Kang
Shanghai Jiao Tong University https://orcid.org/0000-0003-3979-4146
Yan Han
Huazhong University of Science and Technology
Huangwei Zhang
Huazhong University of Science and Technology
Yue Shen
Huazhong University of Science and Technology https://orcid.org/0000-0002-2985-825X
Henghui Xu
Huazhong University of Science and Technology
Zhen Li
Huazhong University of Science and Technology
Yunhui Huang (huangyh@hust.edu.cn)
Huazhong University of Science and Technology https://orcid.org/0000-0003-1687-1938

Article

Keywords: Interfacial self-healing, polymer electrolytes, Li-metal anode, Li-S batteries, solid-state batteries

Posted Date: May 30th, 2023

DOI: https://doi.org/10.21203/rs.3.rs-2924521/v1

Additional Declarations: There is **NO** Competing Interest.

Version of Record: A version of this preprint was published at Nature Communications on January 8th, 2024. See the published version at https://doi.org/10.1038/s41467-023-43467-w.

Abstract

Coupling high capacity cathode and Li metal anode with the solid-state electrolyte has been demonstrated as an effective strategy for increasing the energy density and enhancing the safety of rechargeable batteries. However, the limited ion conductivity of the solid-state electrolyte, the large interfacial resistance of electrode/electrolyte, and the unconstrained dendrite growth of the Li metal anode are still the main challenges hindering the applications of the solid-state Li-metal batteries (SSLMB). Herein, a poly(ether-urethane) based solid-state polymer electrolyte (SPE) with self-healing property are designed to reduce the interface impedance and achieve high performance SSLMB. Benefiting from the dynamic covalent disulfide bonds rearrangement and the hydrogen bonds between urethane groups, the proposed SPE exhibits excellent interfacial self-healing ability, which can help to constantly maintain well interfacial contact between solid-state electrolyte and cathode/anode electrodes during the whole cycling life. By casting the designed SPE directly on the sulfur-based cathodes and Li metal anode, it can be easily prepared the integrated solid-state electrolyte/electrode structures, and then assembled them into full cells. As a result, the Li||Li symmetric cells achieved a long-term cycling stability of more than 6000 h, and the solid-state Li-S batteries show prolonged cycle life of 700 times accompanied with excellent C-rate properties. By using ultrasound imaging technology, it is proved that the interfacial contact of the integrated solid-state electrolyte/electrode structure is much better than traditional laminated ones. The application of the proposed interfacial self-healing SPEs and the integrated electrodes could be easily extended to mass production of high-performance solid-state batteries.

Introduction

Solid-state Li-metal batteries (SSLMB) have received widespread attention due to the high energy density and safety[1–3]. By coupling Li-metal anode with the sulfur-based cathode, the energy density of the full cells can be greatly enhanced[4, 5]. However, the complex and unstable interfacial problems of the electrolyte and electrodes, such as the continuously polysulfide shuttling[6, 7], the rapid consumption of electrolyte and the uncontrollable dendrite growth of Li-metal[8–11, 12], have seriously plagued the commercialization of lithium-sulfur (Li-S) batteries[13, 14].

Upgrading liquid electrolytes with solid-state electrolytes have been considered as an effective strategy to fundamentally solve the inherent safety problems of Li-metal batteries[15–17]. Compared with inorganic solid-state electrolytes (e.g., oxide and sulfide-type solid electrolytes, etc.) which have high ionic conductivity and thermal stability, but are limited by severe mechanical brittleness and high electrolyte/electrode interfacial impedance[3, 18, 19], the solid-state polymer electrolytes (SPEs) are widely studied due to the excellent mechanical flexibility and electrochemical stability[20–22]. As the representative SPEs, the poly(ethylene oxide) (PEO)-based electrolytes are widely studied because of the excellent lithium salt solvation capacity[23]. However, the low Li-ion conductivity caused by highly crystalline, poor mechanical strength, as well as unsatisfactory electrochemical stability, have restrict their further

application[24–26]. In fact, it has been greatly exaggerated that just relying on the flexibility of an all-solid-state polymer electrolyte could totally solve the interface contact problem in SSLAM[24, 27]. When the large interfacial ionic transfer barrier between the solid-state polymer electrolyte and porous electrode was despised, the true ionic conductivity of the polymer electrolyte cannot be fully utilized[28, 29]. The in-situ polymerization strategy has been proved to be an effective method to solve the interface problem of SPEs[30–32]. However, most of the in-situ polymerization reactions are limited by the few choices of the monomer types, and the degree of polymerization is uncontrollable, leading to a gel-state or semi-solid-state of the finial products[33–35]. How to promote the ionic conductivity and construct efficient interfacial ion transport path through ingenious molecular structure remain serious challenges in the field of SSLMB.

Herein, we propose a new class of poly(ether-urethane) based SPEs for constructing integrated SSLMB and achieving excellent electrochemical performance. The abundant ether oxygen (EO – Li^+) and carbonyl oxygen functional groups in the structure promote the dissociation of lithium salts and improve the ionic conductivity. More importantly, during the whole life cycle, the dynamic covalent disulfide bonds and the hydrogen bonds between urethane groups can provide excellent interfacial self-healing capabilities to repair the solid/solid interfacial defects. The ultrasound imaging results show that the interfacial contact of the integrated solid-state electrolyte/electrode structure is much better than traditional laminated ones. As a result, the enhanced interface contact enables the SPAN cathode delivering an extremely long cycling stabilities (93% capacity retention after 700 cycles at 0.3 C) and high rate performance (560 mAh g_{SPAN}^{-1} at 1 C). When matched with the sulfur/carbon black cathode (S@CB), the solid-state Li-S battery can be cycled over 350 times with a high capacity retention of 812 mAh g_S^{-1}.

Results and Discussion

Structure design of SPEs and integrated SSLMB

Poly(ether-urethane) based polymer is usually formed by stepwise polymerization of polyalcohols and polyisocyanates, the repeat functional group of urethano (-NH-COO-) is formed in the main PU framework[36–38]. Polytetrahydrofuran (PTMG) backbone with low molecular weight (2000 g mol^{-1}) and ether-oxygen structure were chosen as the soft segments to dissociate and conduct lithium-ion (Li^+)[39]. The terminal hydroxyl of PTMG can easily react with hexamethylene diisocyanate (HDI) to generate the -NH-COO- (Fig. 1a). On this basis the poly(ether-urethane) with self-healing character (PTMG-HDI-BHDS) was further synthesized by introducing 2-hydroxyethyl disulfide (BHDS) as chain extender, the hydroxyl of the BHDS was further polymerizated with the excess -N = C = O. The repeated reaction nodes of -NH-COO- in the polymer chain are able to form a rich hydrogen bond network[40, 41]. What's more, by introducing dynamic disulfide bond with low bond dissociation energy into poly(ether-urethane) material, the rearrangement of disulfide bond can be realized dynamically at low temperature without external

stimulation, so that the rapid self-healing property of PTMG-HDI-BHDS at room temperature can be achieved (Fig. 1b)[42–45].

In order to show the two completely different battery preparation technology more vividly, the structure of laminated battery and integrated battery from a 3D perspective were compared. By using laminated assembly method, the traditional reported solid-state lithium metal batteries (SSLMB) always show high interface impedance due to the uneven interface and the existence of pore gaps. The dual-integrated strategy of the SSLMB was constructed by using interfacial self-healing SPE (Fig. 1d), the integrated cathode (S@SPE) and integrated anode (Li@SPE) are prepared by pre-impregnation coating method. During the process of solvent volatilization and solidification, the poor contact at the interface of electrolyte/electrode interface are welded together without any gaps, and finally, the self-healing disulfide bond and hydrogen bond at the electrolyte/electrolyte interface is used to solve the multiple interfaces contact problem, which have been plagued in SSLMB for a long time[46].

Materials fabrication and characterization of SPEs

Both of PTMG-HDI and PTMG-HDI-BHDS solutions showed the characteristics of uniform and transparent gel state (Fig. 2a). The difference is that the wall hanging time of PTMG-HDI-BHDS is significantly longer than that of PTMG-HDI, that is because the molecular weight and viscosity of the PTMG-HDI-BHDS were further increased by the introduction of chain extender. The real-time polymerization process of PTMG-HDI-BHDS is traced to measure the average molecular weight (M_n) and viscosity (η) by using gel permeation chromatography (GPC). As shown in the Fig. 2b, the viscosity increases synchronously with the molecular weight during the reaction time for 8 h at 40 ^oC, the M_n and η were finally increased to 7.3 x 10^4 g mol^{-1} and 1.3 x 10^4 cps, respectively.

The homogeneous solution of PTMG-HDI-BHDS was further casted on a polytetrafluoroethylene plate, an optically transparent PTMG-HDI-BHDS film was obtained after the solvent evaporation process (Supplementary Fig. 1). Compared with PEO and PTMG-HDI, the scanning electron microscopy (SEM) images showed that the surface of the as-obtained PTMG-HDI-BHDS film is highly dense and smooth (Supplementary Fig. 2). The crystalline status of the polymers and PTMG-HDI-BHDS/LiFSI electrolyte were analyzed by XRD (Fig. 2c). PEO presented two strong crystal characteristic peaks at about 19.5° and 23.6°. After polymer chain of PTMG-HDI was extended with BHDS, the peak intensities of PTMG-HDI-BHDS and PTMG-HDI-BHDS/LiFSI were obviously reduced, the decreased crystallinity and increased amorphous regions are conducive to improve the Li^+ mobility and enhance the ionic conductivity[47].

The mechanical properties of the as-obtained polymers were compared by characterizing their stress-strain behavior. As shown in the Fig. 2d and 2e, the break strength and ultimate elongation of PTMG-HDI-BHDS were observed to be 88.3 MPa and 2000%, respectively, which were significantly higher than those of PEO (17.8 MPa) and PTMG-HDI (31.2 MPa) (Supplementary Fig. 3)[48–50]. The result should be attributed to the abundant hydrogen bond network and the increased of molecular weight by the chain extender, indicating that the PTMG-HDI-BHDS electrolyte can theoretically act as mechanical barriers for

suppressing Li dendrites growth[51]. The self-healing abilities of PTMG-HDI-BHDS were evaluated vividly by using artificially stained method (Fig. 2f and Supplementary Fig. 4), rhodamine B was added into the colorless PTMG-HDI-BHDS solution to obtain the red film. It was noted that the different colors of PTMG-HDI-BHDS films completely merged into an integral block, and the self-healing interfaces were strong enough to withstand a tensile force along the direction vertical to the cut surface. Furthermore, the self-healing behavior was also confirmed by the observation of the PTMG-HDI-BHDS film after scratched with a scalpel. The optical microscope images showed that the scratches had almost completely disappeared after healing at 30 ^{o}C (Supplementary Fig. 5). The resulting characteristic functional groups were investigated by Fourier-transform infrared spectroscopy (ATR-FTIR) (Fig. 2g). The represented strong stretching vibration peak of C-O-C were appeared around 1102 cm^{-1}, the urethane groups (-NH stretching at 3325 cm^{-1} and C = O stretching at 1719 cm^{-1}) and disulfide bond (around 635 cm^{-1}) can be clearly observed after the polymerization, suggesting the successful synthesis of PTMG-HDI-BHDS. The peak of -C = O group is obviously split into two peaks, one of which is blue shifted to around 1680 cm^{-1} due to the formation of the strong hydrogen bonds between -NH-COO- (Fig. 2g and Supplementary Fig. 6).

1H NMR spectra were recorded by using $CDCl_3$ as a solvent to elucidate the structural composition of the PTMG-HDI and PTMG-HDI-BHDS (Fig. 2h and Supplementary Fig. 7). The strong signal chemical shift at 3.43 and 1.63 ppm is assigned to the H on dominant group -O-CH_2-CH_2-CH_2-CH_2-O- in PTMG. The integral area ratio of 1:1:1 of the chemical shift at 3.17, 1.51 and 1.35 ppm was matched well with the repeating unit structure of HDI (Supplementary Fig. 8). The integral area ratio of 1:1 of the chemical shift at 4.08 and 2.94 ppm in PTMG-HDI-BHDS matched well with the -CH_2-CH_2-S- in BHDS (Fig. 2h), implying that the chain extender was successfully introduced in the polymer framework.

High resolution X-ray photoelectron spectroscopy (XPS) of C 1s, N1s and survey spectrum were displayed in Fig. 2i-j and Supplementary Fig. 9. The strength of N1s peak in PTMG-HDI-BHDS was significantly higher than that in PTMG-HDI, and a new peak of disulfide bond (163.4 eV) was emerging, indicating that the reaction of chain extender further increased with the urethane content. The C1s spectrum (Fig. 2j) can be deconvoluted into C-C (284.8 eV), C-O-C (286.2 eV), and C = O (288.9 eV), respectively, agreeing well with the molecular structure of PTMG-HDI-BHDS (Fig. 2h).

Electrochemical characterization of the SPEs

The Li^+ conductivity properties of different SPEs from 25 to 80 ^{o}C were presented in Fig. 3a and Supplementary Fig. 10. With a weight ratio of polymer : LiFSI = 2 : 1, the dual-integrated SS|PTMG-HDI-BHDS|SS (SS stands for sheet steel) cell was assembled by fitting two integrated SS@SPE together, the total thickness of the bonded SPE was about 200 μm to reduce the measurement error (Supplementary Fig. 11). The PTMG-HDI-BHDS/LiFSI (2.4×10^{-4} S cm^{-1}) exhibited a significantly higher ionic conductivity than the PEO/LiFSI (1.2×10^{-5} S cm^{-1}) and PTMG-HDI/LiFSI (6.5×10^{-5} S cm^{-1}) at 30 ^{o}C, indicating that the strong interface self-healing and adhesion properties can significantly decrease the interfacial impedance between the SS@SPEs, and the amorphous polymer skeleton could construct fast Li^+ transport paths. The ionic conductivities at different temperatures were presented in Fig. 3b, the lower

activation energy of PTMG-HDI-BHDS/LiFSI (Ea = 0.30 eV) in the Arrhenius plots reflected a lower Li^+ migration barrier than that of PTMG-HDI/LiFSI and PEO/LiFSI, this is helpful to improve the rate performance of the battery.

Raman spectra was used to further evaluate the dissociation capabilities of LiFSI in the SPEs[52]. the peaks of S – N–S of FSI^- located at 721, 744 and 773 cm^{-1} can be divided into free FSI^- ions (completely dissolved in water), contact ion pairs (CIP), and undissociated LiFSI, respectively (Fig. 3c,). The solvation structures of LiFSI in three SPEs were differentiate by comparing the integral percentage of each peak area. The PEO/LiFSI showed a dominating mount of CIPs and very limited free FSI^- because of the relatively weak dissociation capacity of PEO[47]. In stark contrast, the S – N–S peak in PTMG-HDI-BHDS/LiFSI underwent a significant shift to 721 cm^{-1}, the proportions of free FSI^- went up from 68.5% (PTMG-HDI/LiFSI) to 95.2% (PTMG-HDI-BHDS/LiFSI), indicating that the low crystallinity of PTMG-HDI-BHDS contributed to a high degree dissociation of FSI^-. The LUMO energy of the repeating units in PTMG (1.35 eV) is significantly higher than that of the PEO repeating units (0.64 eV), indicating stronger electrochemical compatibility of the PTMG-HDI-BHDS with Li anode (Fig. 3d)[53]. High binding energy of PTMG ($\triangle E_{PTMG}$ = -0.83 eV) with Li^+ than that of PEO ($\triangle E_{PEO}$ = -0.75 eV) promoted the PTMG-HDI-BHDS thermodynamically coordinating with Li^+, this result was beneficial to the solvation and dissociation of Li^+.

As shown in Fig. 3e, the linear sweep voltammetry (LSV) curves of asymmetrical cells indicated that PTMG-HDI-BHDS/LiFSI displayed a more wide electrochemical voltage above 5.0 V when compared with PEO (3.8 V) and PTMG-HDI (4.1 V), the improved interfacial electrochemistry stability of PTMG-HDI-BHDS/LiFSI is attributed to the adjacent electro-pumping group of urethano, effectively suppressing the decomposition of circumjacent E-O segments. Besides, an exceptionally high Li^+ transference number (t_{Li}^+ = 0.81) of PTMG-HDI-BHDS/LiFSI can inhibit the formation of space charge near Li anode and further reduce the dendrite formation under high current density (Fig. 3f).

Electrochemical stability of the Li|SPEs|Li symmetric cells

Ultrasound imaging technology has been proved to be a powerful tool to evaluate the quality of interfacial contacts and side reactions due to the high sensitivity to gas/vacuum[54, 55]. The peak-peak amplitude values (PPV) between the recorded maximum and minimum signal are converted into different colors ranging from blue to red to create the ultrasonic image. Ultrasonic imaging was carried out during the galvanostatic cycling of the Li|SPEs|Li pouch cells at 0.2 mA cm^{-2} (Fig. 4a-4f and Supplementary Fig. 12). A large blue area appeared around the surrounding edges of the laminated Li|PEO|Li pouch cells and then the area expanded rapidly with cycling, the PPV decreased from 0.11 to 0.06 V, this phenomenon was caused by the invalid interface contact and sustaining Li dendrite growth (Fig. 4a-4c and Supplementary Fig. 13). In stark contrast, the integrated Li@SPE was prepared by coating electrolyte solution onto Li anode and dried in the argon-filled glove box (Supplementary Fig. 14). By sticking the two Li@SPE together, the overpotential of the dual-integrated Li|PTMG-HDI-BHDS|Li pouch cell gradually

decreased first and then remained stable during the first 10 cycles (Supplementary Fig. 15). The ultrasonic images showed a gradual increase PPV from 0.57 to 0.62 V, along with a gradual change in color from green to yellow, indicating that the interfaces of integrated Li@SPE can be completely self-healed together by dynamic disulfide bonds and hydrogen bonds, promoting the formation of the stable and dense SEI film (Fig. 4d-4f).

According to the above conclusions, Li|SPEs|Li symmetric coin cells were assembled comparatively to investigate the long-term cycling stability and rate performance (Fig. 4g and Supplementary Fig. 16). The Li|PTMG-HDI-BHDS|Li cell assembled by two Li@SPE exhibited an outstanding stable voltage hysteresis for more than 6000 h (3000 cycles) under a current density of 0.2 mA cm^{-2}, indicating an excellent good interfacial compatibility and electrochemical stability, better than many of the reported SPEs (Supplementary Table 1). The rate capabilities of the integrated Li|PTMG-HDI-BHDS|Li cells were further tested by cycling from 0.1 to 1.0 mA cm^{-2} with an areal capacity from 0.5 to 5.0 mAh cm^{-2} (Fig. 4h). The lowest overpotentials of 49, 74, 113, 172, 233, and 262 mV were obtained at the current densities of 0.1, 0.2, 0.4, 0.6, 0.8, and 1.0 mA cm^{-2}, this is mainly due to the high ionic conductivity and stable self-healing interface formed in the cell. In sharp contrast, the Li|PEO|Li and Li|PTMG-HDI|Li cells showed an abrupt failure under a current density of 0.4 mA cm^{-2}. The uniform morphology of the Li deposition layer can be achieved even at a high rate test in Li|PTMG-HDI-BHDS|Li cells. In comparison, irregular dendrite-like domains were observed on the surface of Li anodes with PEO/LiFSI and PTMG-HDI/LiFSI in the top view and cross-sectional SEM images (Supplementary Fig. 17 and Supplementary Fig. 18).

XPS was performed by Ar^+ sputtering for 0, 50, 100 and 200 s on the Li anode after the rate performance test, further investigating the chemical compositions of the SEI layers. As shown in Fig. 4i and 4j, high concentration of organic C-F (72%) at 688.1 eV with less inorganic Li-F (28%) at 685.0 eV in the F1s spectra was observed in Li|PEO|Li. With the increase of etching depth, the content of organic was obviously higher than that in Li|PTMG-HDI-BHDS|Li due to the continuous decomposition of the unstable electrolyte. The non-uniform organic-inorganic compositions also induced a highly inhomogeneous stress and strain when the electrode volumetric expanded during cycling. Consequently, the repeated breaking and reforming of SEI leaded to a low Coulombic efficiency and poor stability. For the Li anode cycled with PTMG-HDI-BHDS/LiFSI, a small quantity of C-F (6%) and a significantly high content of Li-F (94%) were observed before etching, this phenomenon became more obvious during the deep etching. As previously reported, LiF is considered as an excellent electronic insulator with high interfacial energy for Li^+, which could promote migration of Li^+ through the SEI and stabilize the interface of Li anode[30, 56–58]. This result suggests that the decomposition of the polymer electrolyte is well suppressed and the decomposition of LiFSI contributes greatly to the formation of SEI.

Electrochemical Performance of the solid-state Li-S batteries

The solution of PTMG-HDI-BHDS/LiFSI exhibited favorable wettability toward anode/cathode (Supplementary Fig. 19). The precursor solutions were further sufficiently infiltrated into the porous S

cathodes, the integrated SPAN@SPE and Li@SPE were formed simultaneously after the solvent evaporation (Supplementary Fig. 20 and Supplementary Fig. 21). The SPAN|PTMG-HDI-BHDS|Li cells were assembled by simply fitting the integrated SPAN@SPE with Li@SPE together. As shown in Fig. 5a and Supplementary Fig. 22, after activation at 0.05 C (1 C = 1000 mAh g_{SPAN}^{-1}) between 1.0 and 3.0 V, SPAN|PTMG-HDI-BHDS|Li delivered an initial discharge capacity of 602 mAh g_{SPAN}^{-1} at 0.3 C. After 400 cycles, the discharge capacities of 606, 180, and 124 mAh g_{SPAN}^{-1} were maintained for the SPAN|PTMG-HDI-BHDS|Li, SPAN|PTMG-HDI |Li, and SPAN|PEO|Li cells, accounting for ~ 100%, 31%, and 30% of their initial capacities at 0.3 C, respectively. A reversible discharge capacity of 560 mAh g_{SPAN}^{-1} with a Coulombic efficiency above 99% was still retained after 700 cycles by using PTMG-HDI-BHDS electrolyte. The high cycling stability (93% capacity retention) are significantly superior to most solid-state Li-S batteries reported so far (Supplementary Table 2). The rate performance of the integrated SPAN|SPEs|Li cell was further evaluated at different current densities ranging from 0.1 to 1.0 C (Fig. 5b and 5c). The discharge capacities of SPAN|PTMG-HDI-BHDS|Li cell from 0.1 to 1.0 C were 641, 611, 594, 588, 582, 576, 570, 563, and 557 mAh g_{SPAN}^{-1}, respectively. When the current density was switched back to 0.1 C, a high discharge capacity was recovered and maintained for the next 200 cycles, which was significantly better than those of the laminated SPAN|PEO|Li and integrated SPAN|PTMG-HDI|Li cells at all tested rates.

The cycling performance of the S|PTMG-HDI-BHDS|Li pouch cell was further investigated. The digital image showed that the cell battery can normally power LED lamps under room temperature (Fig. 5d, Supplementary Fig. 23 and Supplementary Fig. 24). The total discharge capacity in the first cycle was as high as 216 mAh (611.8 mAh g_{SPAN}^{-1}) at 0.3 C, the cell exhibited a discharge capacity of 561 mAh g_{SPAN}^{-1} with 91.7% capacity retention after 250 cycles.

To demonstrate the application feasibility of the PTMG-HDI-BHDS/LiFSI to simultaneously overcome the polysulfide shuttling and Li dendrite issues, S-based cathode (S@CB) was prepared by using commercial carbon black (CB) as the sulfur host, which is well known for its significant capacity attenuation in liquid electrolyte[11]. The capacities and cycling stabilities of the Li-S cells with 2.0 mg cm^{-2} of sulfur were evaluated at a current density of 0.3 C (1 C = 1675 mA g_S^{-1}) and the specific capacities were calculated based on the weight of sulfur. All the cells were first activated at 0.05 C for one cycle (Fig. 5e). The laminated S@CB|PEO|Li and integrated S@CB|PTMG-HDI|Li cells exhibited a capacity of 282 and 483 mAh g_S^{-1} with 43.0% and 57.4% capacity retention after 350 cycles, respectively. The poor cycling stabilities of these two cells are mainly caused by ineffective interface contact and low ionic conductivity. The shuttling effects remained a serious problem in PEO-based electrolytes because of the similar molecular structure to ether-based electrolyte[59]. The SPAN|PTMG-HDI-BHDS|Li cell after activation showed the highest initial capacity (962 mAh g_S^{-1}), a reversible capacity of 812 mAh g_S^{-1} (ca. 1.6 mAh cm^{-2}) was still retained with 84.4% capacity retention after 350 cycles at 0.3 C (Supplementary Fig. 25). The PTMG-HDI-BHDS/LiFSI with relatively low concentration of ether-oxygen structure can effectively suppress the shuttling of polysulfides, agreeing well with the high capacity retention.

Mechanism analysis of the stable interfaces in solid-state pouch cells

In order to prove the concept of dual-integrated electrodes to construct interfacial self-healing solid-state Li-S batteries, the cross-sectional SEM images and EDS mapping of pouch cells indicated that SPAN@SPE and Li@SPE layers were well integrated without any visible delamination (Fig. 6a-6c). PTMG-HDI-BHDS/LiFSI was served as both electrolyte and Li^+ conductor binder in the SPAN@SPE, S element is mainly derived from SPAN and LiFSI, LiFSI is distributed in both the SPAN@SPE layer and the Li@SPE layer, providing rich channels for the transmission of Li^+ ions[4]. The self-healing interface can be clearly observed in the enlarged SEM image (Fig. 6d), visually illustrating the 3D interpenetrating Li^+ channel between SPAN@SPE and Li@SPE. This ingenious strategy would sharply reduce the interfacial contact resistance and realize the rapid transmission of Li^+ (Supplementary Fig. 26).

Figure 6e illustrated the assembly process of the laminated SPAN|PEO|Li pouch cell, compared with the soft Li anode, the porous cathode faced more severe interfacial problems, this contrast was further evaluated by the ultrasonic imaging. The region of the Al-plastic film appears red with a PPV of 0.89 V, when the SPAN|PEO|Li was assembled by using the laminated strategy, the poor contact at the PEO/LiFSI interface can dramatically decrease the ultrasonic signal, resulting in an obvious large area of dark blue ultrasonic image with a PPV of 0.05 V (Fig. 6e and 6f). In subsequent cycles, the blue area gradually expanded to the entire cell area due to continuous uneven deposition of Li. In stark contrast, the region of the integrated SPAN|PTMG-HDI-BHDS|Li appeared uniform green color in the initial state, a gradual increase of PPV from 0.58 to 0.65 V in the next 50 cycles, along with change in color from green to yellow (Fig. 6g and 6h), indicating a gradually better contact interface in SPAN|PTMG-HDI-BHDS|Li cell during the cycling.

Conclusions

In summary, we developed a facile route to construct poly(ether-urethane) based electrolyte with self-healing properties, which can be casted directly on the electrode films to construct the integrated solid-state electrode/electrolyte. Benefit from the dynamic covalent disulfide bonds rearrangement and the hydrogen bonds between urethane groups, the interface of two integrated electrodes can be self-healed to solve the problem of multiple interface contact in SSLMB. The constructed SPEs delivered robust mechanical strength, excellent ion conductivity, high Li^+ transference number, and broadened electrochemical stability window. The long-term cycling stability of Li|PTMG-HDI-BHDS|Li symmetric cells were investigated for more than 6000 h. Remarkably, the enhanced interface contact enabled the SPAN and S@CB cathodes delivering an extremely long cycling stabilities and high capacity retention. The integrated SSLMB constructed by self-healing SPEs based on dynamic disulfide bonds opens a new promising approach for constructing high-performance SSLMB.

Methods

Preparation of PTMG-HDI

The PTMG-HDI was synthesized based on a condensation reaction of PTMG with HDI. Briefly, 2.5 g PTMG and 250 μL HDI were dissolved in 5 mL CH_2Cl_2. 5 μL DBTDL was added to the solution as a reaction catalyst. The mixture was stirred at 40 ^oC for 3 h in an N_2-filled glove box. Then 5 mL DMAc was added into the reaction mixture every 2 h for 3 times and stirred for 12 h. Finally, a transparent PTMG-HDI solution was obtained.

Preparation of PTMG-HDI-BHDS

The synthesis of PTMG-HDI-BHDS is based on the introduction of chain extender BHDS into the reaction of PTMG-HDI. Briefly, 2.5 g PTMG, 500 μL HDI and 5 μL DBTDL were dissolved in 5 mL CH_2Cl_2 and stirred at 40 ^oC for 1 h, then 200 μL BHDS was added into above reaction solution. Subsequently, 5 mL DMAc was added into the reaction mixture every 2 h for 3 times and stirred for 12 h to obtain the PTMG-HDI-BHDS solution.

Preparation of PEO/LiFSI, PTMG-HDI/LiFSI and PTMG-HDI-BHDS/LiFSI electrolytes

The poly(ethylene oxide) (PEO, Mw = 6×10^6 g mol^{-1}) and lithium bis(fluorosulfonyl)imide (LiFSI) with a mass ratio of 2 : 1 were dissolved into acetonitrile to form a uniform PEO/LiFSI solution. The PTMG-HDI and PTMG-HDI-BHDS polymer solutions were mixed with LiFSI in the dimethylacetamide (DMAc) solvent with a mass ratio of 2 : 1 and stirred for 3 h. These viscous solutions were degassed in vacuum environment and casted into a Teflon mold, then dried in a vacuum oven at 65°C for 48 h to obtain the PEO/LiFSI, PTMG-HDI/LiFSI and PTMG-HDI-BHDS/LiFSI electrolytes.

Preparation of the SPAN and S@CB

SPAN was synthesized according to a modified method previously reported[60]. 1.0 g polyacrylonitrile (PAN) and 3.5 g S powder were mixing uniformity in 10 mL ethanol by high-energy ball milling for 4 h. Then the SPAN with a sulfur content of 45.0 wt% was obtained by heated composite at 300 ^oC for 450 minutes in N_2 atmosphere. The S@CB composite with a sulfur content of 80 wt% was prepared by the melt diffusion method[11].

Electrochemical Characterizations

For electrode fabrication, the cathode slurry was obtained by mixing the SPAN or S@CB, CB, SPEs and PVDF with a weight ratio of 80 : 10 : 5 : 5 in DMAc. The as-obtained slurry was then coated onto carbon-coated Al foil, dried at 65 ^oC in vacuum with a mass loading of 2.0 ~ 2.2 mg cm^{-2} SPAN or sulfur. The integrated cathode@SPEs and Li@SPEs were prepared by cast aforesaid polymer electrolyte solutions onto the cathodes and drying in vacuum at 65 ^oC for 48 h. For the pouch cells, the integration cathode and anode were punched into rectangle with 50 mm × 60 mm. All the components were assembled in an argon-filled glove box (H2O < 0.1 ppm and O2 < 0.1 ppm). A CHI760E electrochemical workstation was

used for the tests of the intrinsic electrochemical properties. The galvanostatic measurements tests for coin-type and pouch-type cells were conducted on the NEWARE battery test instrument within a cutoff voltage window of 1.0 ~ 3.0 V.

Declarations

Acknowledgements

This work is supported by the National Key R&D Program of China (Grant No. 2021YFB2400300), the National Natural Science Foundation of China (Grant Nos. 52202236, 5202780089, 52231009 and 51972131), and China Postdoctoral Science Foundation (Grant No. 2022M711232). The authors thank the Analytical and Testing Center of Huazhong University of Science and Technology (HUST) and State Key Laboratory of Materials Processing and Die & Mould Technology for characterizations. Thanks eceshi (www.eceshi.com) for the XPS test.

Author contributions

F.P., Z.L. and Y.H. conceived and designed the research; F.P., L.W. and Y.Z. performed the experiments and the characterization of the materials; Y.L. and H.H. conducted part of the characterizations; H.Z. and Q.K. performed part of synthesis and electrochemical tests; Y.S. and H.X. made instructive advice to revise the full text; F.P., Z.L. and Y.H. analyzed all the data and co-wrote the paper. All authors contributed to the discussion of the manuscript.

Competing interests

The authors declare no competing interests.

Reporting summary

Further information on research design is available in the Nature Portfolio Reporting Summary linked to this article.

Data availability

The data that support the findings of this study are available from the corresponding authors upon reasonable request.

References

1. Zhao, Q., Stalin, S., Zhao, C. & Archer, L. A. Designing solid-state electrolytes for safe, energy-dense batteries. *Nat. Rev. Mater.* **5**, 229-252 (2020).
2. Judez, X., Gebresilassie Eshetu, G., Li, C., Rodriguez-Martinez, L. M., Zhang, H. & Armand, M. Opportunities for rechargeable solid-state batteries based on Li-intercalation cathodes. *Joule* **2**, 2208-

2224 (2018).

3. Ning, Z. et al. Visualizing plating-induced cracking in lithium-anode solid-electrolyte cells. *Nat Mater* **20**, 1121-1129 (2021).
4. Chen, X. Z., He, W. J., Ding, L. X., Wang, S. Q. & Wang, H. H. Enhancing interfacial contact in all solid state batteries with a cathode-supported solid electrolyte membrane framework. *Energy Environ. Sci.* **12**, 938-944 (2019).
5. Lei, D. et al. Progress and perspective of solid-state lithium-sulfur batteries. *Adv. Funct. Mater.* **28**, 1707570 (2018).
6. Pei, F. et al. Self-supporting sulfur cathodes enabled by two-dimensional carbon yolk-shell nanosheets for high-energy-density lithium-sulfur batteries. *Nat. Commun.* **8**, 482 (2017).
7. Xing, C. et al. Regulating liquid and solid-state electrolytes for solid-phase conversion in Li-S batteries. *Chem* **8**, 1201-1230 (2022).
8. Xie, J. et al. Engineering stable interfaces for three-dimensional lithium metal anodes. *Sci. Adv.* **4**, eaat5168 (2018).
9. Kim, M. S. et al. Langmuir-Blodgett artificial solid-electrolyte interphases for practical lithium metal batteries. *Nat. Energy* **3**, 889-898 (2018).
10. Yujing Liu et al. Self-assembled monolayers direct a LiF-rich interphase toward long-life lithium metal batteries. *Science* **375**, 739-745 (2022).
11. Pei, F. et al. Titanium-oxo cluster reinforced gel polymer electrolyte enabling lithium-sulfur batteries with high gravimetric energy densities. *Energy Environ. Sci.* **14**, 975-985 (2021).
12. Cha, E. et al. 2D MoS_2 as an efficient protective layer for lithium metal anodes in high-performance Li-S batteries. *Nature Nanotechnology* **13**, 337-344 (2018).
13. Yang, X., Luo, J. & Sun, X. Towards high-performance solid-state Li-S batteries: from fundamental understanding to engineering design. *Chem. Soc. Rev.* **49**, 2140-2195 (2020).
14. Xu, L. et al. Toward the scale-up of solid-state lithium metal batteries: The gaps between lab-level cells and practical large-format batteries. *Adv. Energy Mater.* **11**, 2002360 (2021).
15. Famprikis, T., Canepa, P., Dawson, J. A., Islam, M. S. & Masquelier, C. Fundamentals of inorganic solid-state electrolytes for batteries. *Nat Mater* **18**, 1278-1291 (2019).
16. Wan, J. et al. Ultrathin, flexible, solid polymer composite electrolyte enabled with aligned nanoporous host for lithium batteries. *Nat. Nanotechnol.* **14**, 705-711 (2019).
17. Janek, J. & Zeier, W. G. Challenges in speeding up solid-state battery development. *Nat. Energy*, 8, 230–240 (2023).
18. Fu, K. et al. Three-dimensional bilayer garnet solid electrolyte based high energy density lithium metal-sulfur batteries. *Energy Environ. Sci.* **10**, 1568-1575 (2017).
19. Kwok, C. Y., Xu, S. Q., Kochetkov, I., Zhou, L. D. & Nazar, L. F. High-performance all-solid-state Li_2S batteries using an interfacial redox mediator. *Energy Environ. Sci.* **16**, 610-618 (2023).

20. Zhou, D., Shanmukaraj, D., Tkacheva, A., Armand, M. & Wang, G. Polymer electrolytes for lithium-based batteries: Advances and prospects. *Chem* **5**, 2326-2352 (2019).
21. Li, C. et al. A quasi-intercalation reaction for fast sulfur redox kinetics in solid-state lithium-sulfur batteries. *Energy Environ. Sci.* **15**, 4289-4300 (2022).
22. Chi, S.-S., Liu, Y., Zhao, N., Guo, X., Nan, C. W. & Fan, L. Z. Solid polymer electrolyte soft interface layer with 3D lithium anode for all-solid-state lithium batteries. *Energy Storage Mater.* **17**, 309-316 (2019).
23. Xu, H. et al. High-performance all-solid-state batteries enabled by salt bonding to perovskite in poly(ethylene oxide). *Proc. Natl Acad. Sci. USA* **116**, 18815-18821 (2019).
24. Fan, L. Z., He, H. C. & Nan, C. W. Tailoring inorganic-polymer composites for the mass production of solid-state batteries. *Nat. Rev. Mater.* **6**, 1003-1019 (2021).
25. Ji, Y. et al. PIM-1 as a multifunctional framework to enable high-performance solid-state lithium-sulfur batteries. *Adv. Funct. Mater.* **31**, 2104830 (2021).
26. Yang, X. F. et al. Determining the limiting factor of the electrochemical stability window for PEO-based solid polymer electrolytes: main chain or terminal -OH group? *Energy Environ. Sci.* **13**, 1318-1325 (2020).
27. Zhang, M. et al. Wetting phenomena and their effect on the electrochemical performance of surface-tailored lithium metal electrodes in contact with cross-linked polymeric electrolytes. *Angew. Chem. Int. Ed.* **59**, 17145-17153 (2020).
28. Wang, W.-P. et al. Solidifying cathode-electrolyte interface for lithium-sulfur batteries. *Adv. Energy Mater.* **11**, 2000791 (2021).
29. Dong, D. et al. Polymer electrolyte glue: A universal interfacial modification strategy for all-solid-state Li batteries. *Nano letters* **19**, 2343-2349 (2019).
30. Zhao, Q., Liu, X., Stalin, S., Khan, K. & Archer, L. A. Solid-state polymer electrolytes with in-built fast interfacial transport for secondary lithium batteries. *Nat. Energy* **4**, 365-373 (2019).
31. Cho, Y. G., Hwang, C., Cheong, D. S., Kim, Y. S. & Song, H. K. Gel/solid polymer electrolytes characterized by in situ gelation or polymerization for electrochemical energy systems. *Adv. Mater.* **31**, 1804909 (2019).
32. Chai, J. et al. In situ generation of poly (vinylene carbonate) based solid electrolyte with interfacial stability for $LiCoO_2$ lithium batteries. *Adv. Sci.* **4**, 1600377 (2017).
33. Feng-Quan Liu et al. Upgrading traditional liquid electrolyte via in situ gelation for future lithium metal batteries. *Sci. Adv.* **4**, eaat5383 (2018).
34. Xiang, J. et al. A flame-retardant polymer electrolyte for high performance lithium metal batteries with an expanded operation temperature. *Energy Environ. Sci.* **14**, 3510-3521 (2021).
35. Wang, Y., Chen, S., Li, Z., Peng, C., Li, Y. & Feng, W. In-situ generation of fluorinated polycarbonate copolymer solid electrolytes for high-voltage Li-metal batteries. *Energy Storage Mater.* **45**, 474-483 (2022).

36. Engels, H. W. et al. Polyurethanes: versatile materials and sustainable problem solvers for today's challenges. *Angew. Chem. Int. Ed.* **52**, 9422-9441 (2013).
37. Tang, S. et al. A novel cross-linked nanocomposite solid-state electrolyte with super flexibility and performance for lithium metal battery. *Nano Energy* **71**, 104600 (2020).
38. Guo, H., Han, Y., Zhao, W., Yang, J. & Zhang, L. Universally autonomous self-healing elastomer with high stretchability. *Nat. Commun.* **11**, 2037 (2020).
39. Mackanic, D. G. et al. Crosslinked poly(tetrahydrofuran) as a loosely coordinating polymer electrolyte. *Adv. Energy Mater.* **8**, 1800703 (2018).
40. Wu, N. et al. Self-healable solid polymeric electrolytes for stable and flexible lithium metal batteries. *Angew. Chem. Int. Ed.* **58**, 18146-18149 (2019).
41. Xu, J., Chen, J., Zhang, Y., Liu, T. & Fu, J. A fast room-temperature self-healing glassy polyurethane. *Angew. Chem. Int. Ed.* **60**, 7947-7955 (2021).
42. Zhang, Q. et al. Thermal-triggered dynamic disulfide bond self-heals inorganic perovskite solar cells. *Angew. Chem. Int. Ed.* **61**, e202116632 (2022).
43. Cho, D. H. et al. Self-healable, stretchable, and nonvolatile solid polymer electrolytes for sustainable energy storage and sensing applications. *Energy Storage Mater.* **45**, 323-331 (2022).
44. Kim, S. M. et al. Superior toughness and fast self-healing at room temperature engineered by transparent elastomers. *Adv. Mater.* **30**, 1705145 (2018).
45. Lai, Y., Kuang, X., Zhu, P., Huang, M., Dong, X. & Wang, D. Colorless, transparent, robust, and fast scratch-self-healing elastomers via a phase-locked dynamic bonds design. *Adv. Mater.* **30**, 1802556 (2018).
46. Narayan, R., Laberty-Robert, C., Pelta, J., Tarascon, J. M. & Dominko, R. Self-healing: An emerging technology for next-generation smart batteries. *Adv. Energy Mater.* **12**, 2102652 (2022).
47. Lin, D. C. et al. High ionic conductivity of composite solid polymer electrolyte via in situ synthesis of monodispersed SiO_2 nanospheres in poly(ethylene oxide). *Nano Lett* **16**, 459-465 (2016).
48. Wang, H. et al. Thiol-branched solid polymer electrolyte featuring high strength, toughness, and lithium ionic conductivity for lithium-metal batteries. *Adv. Mater.* **32**, e2001259 (2020).
49. Mackanic, D. G. et al. Decoupling of mechanical properties and ionic conductivity in supramolecular lithium ion conductors. *Nat. Commun.* **10**, 5384 (2019).
50. Ou, Y., Zhao, T., Zhang, Y., Zhao, G. & Dong, L. Stretchable solvent-free ionic conductor with self-wrinkling microstructures for ultrasensitive strain sensor. *Mater. Horiz.* **9**, 1679-1689 (2022).
51. Rekondo, A., Martin, R., Ruiz de Luzuriaga, A., Cabañero, G., Grande, H. J. & Odriozola, I. Catalyst-free room-temperature self-healing elastomers based on aromatic disulfide metathesis. *Mater. Horiz.* **1**, 237-240 (2014).
52. Liu, W. et al. Designing polymer-in-salt electrolyte and fully infiltrated 3D electrode for integrated solid-state lithium batteries. *Angew. Chem. Int. Ed.* **60**, 12931-12940 (2021).

53. Pan, X. Y. et al. High voltage stable polyoxalate catholyte with cathode coating for all-solid-state Li-metal/NMC622 batteries. *Adv. Energy Mater.* **10**, 2002416 (2020).
54. Deng, Z. et al. Ultrasonic scanning to observe wetting and “unwetting” in Li-ion pouch cells. *Joule* **4**, 2017-2029 (2020).
55. Huo, H. et al. Evaluating interfacial stability in solid-state pouch cells via ultrasonic imaging. *ACS Energy Lett.* **7**, 650-658 (2022).
56. Jiao, S. et al. Stable cycling of high-voltage lithium metal batteries in ether electrolytes. *Nat. Energy* **3**, 739-746 (2018).
57. Gebresilassie Eshetu, G. et al. Ultrahigh performance all solid-state lithium sulfur batteries: Salt anion's chemistry-induced anomalous synergistic effect. *J. Am. Chem. Soc.* **140**, 9921-9933 (2018).
58. Gao, Y. et al. Polymer-inorganic solid-electrolyte interphase for stable lithium metal batteries under lean electrolyte conditions. *Nat Mater* **18**, 384-389 (2019).
59. Fang, R., Xu, H., Xu, B., Li, X., Li, Y. & Goodenough, J. B. Reaction mechanism optimization of solid-state Li-S batteries with a PEO-based electrolyte. *Adv. Funct. Mater.* **31**, 2001812 (2020).
60. Wang, C. et al. Solid-state plastic crystal electrolytes: Effective protection interlayers for sulfide-based all-solid-state lithium metal batteries. *Adv. Funct. Mater.* **29**, 1900392 (2019).

Figures

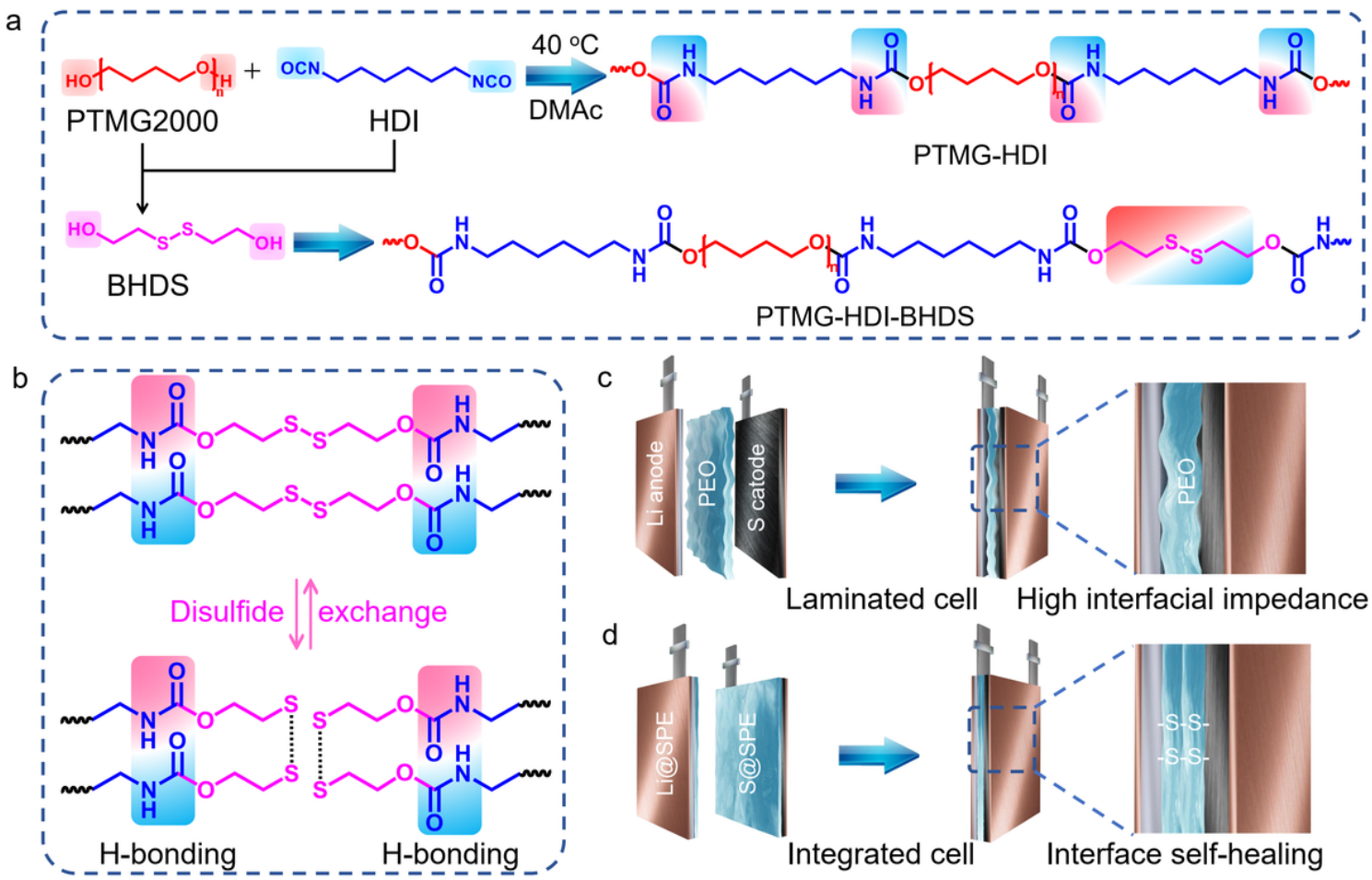

Figure 1

Schematic illustration of the polymer electrolyte structure and the structural comparison of solid-state Li-S batteries. a Chemical structure of the PTMG-HDI and PTMG-HDI-BHDS. **b** Schematic structure of the dynamic covalent disulfide bond and hydrogen bond in PTMG-HDI-BHDS. **c** The structure of conventional laminated solid-state battery. **d** The structure of integrated electrode/electrolyte and the solid-state Li-S battery.

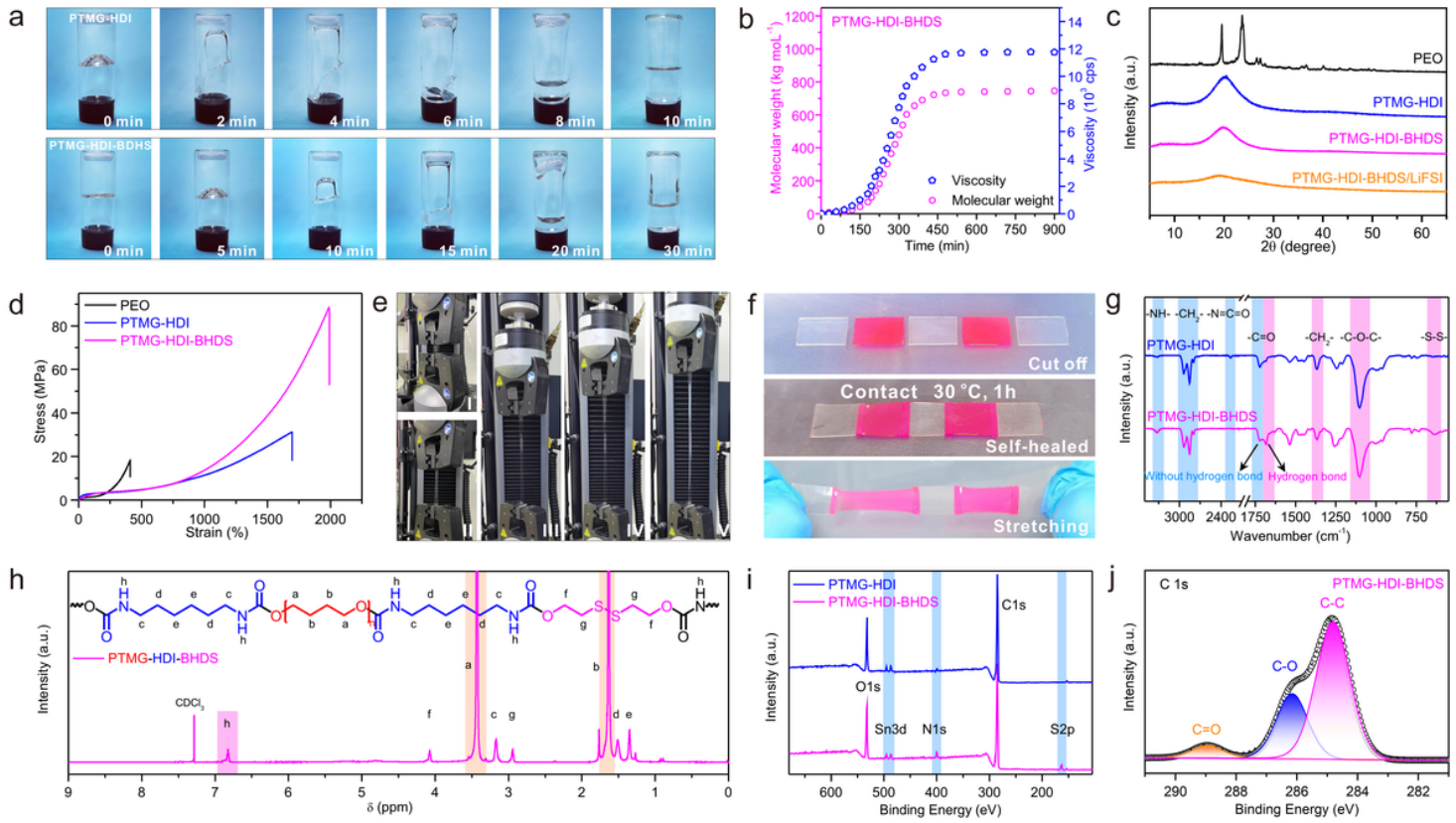

Figure 2

Structural characterization of polymer electrolytes. a Viscosity contrast optical photographs of the PTMG-HDI and PTMG-HDI-BHDS after polymerization. **b** Variation processes of molecular weight (red point) and viscosity (blue point) during polymerization process. **c** XRD patterns of the polymers and PTMG-HDI-BHDS/LiFSI. **d** The stress-strain curves of the polymers. **e** Photographs of the stress-strain measurement of PTMG-HDI-BHDS. **f,** The interfacial self-healing process of PTMG-HDI-BHDS. **g** ATR-FTIR spectra of the PTMG-HDI and PTMG-HDI-BHDS. **h** ^{1}H NMR spectrum of the PTMG-HDI-BHDS in $CDCl_3$ (500 MHz). **i** The comparison of XPS survey spectrums. **j** C 1s spectra of the PTMG-HDI-BHDS.

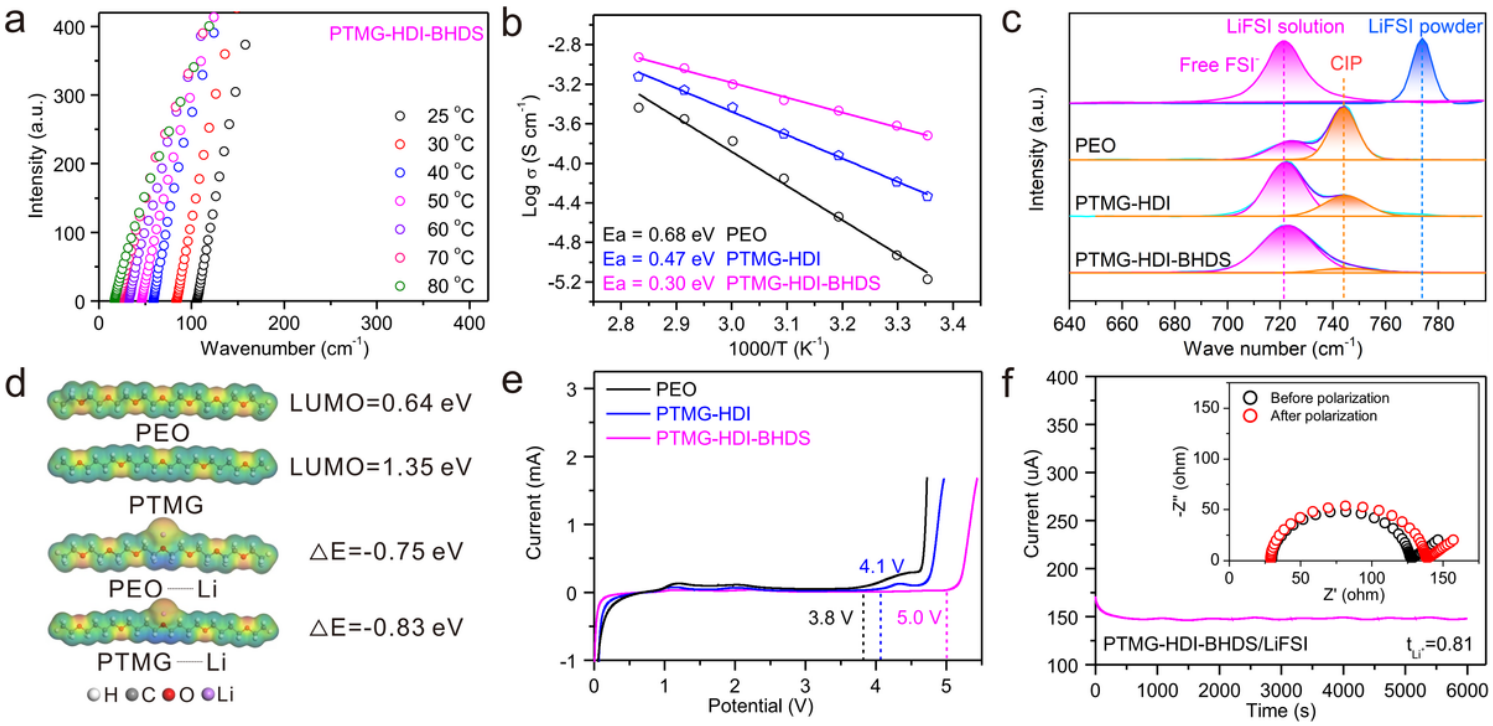

Figure 3

Electrochemical characterization of the SPEs. a EIS measurements of the PTMG-HDI-BHDS/LiFSI at different temperatures. **b** Temperature-dependent ionic conductivities of the SPEs. **c** Raman spectra and the corresponding fitting curves of the S-N-S stretching vibrational mode in the SPEs. **d** Calculated LUMOs of PEO and PTMG and their binding energy with Li^+. **e** Linear scan voltammetry curves of the SPEs. **f** Chronoamperometry curve and AC impedance spectra before and after polarization of Li|PTMG-HDI-BHDS|Li symmetric cell.

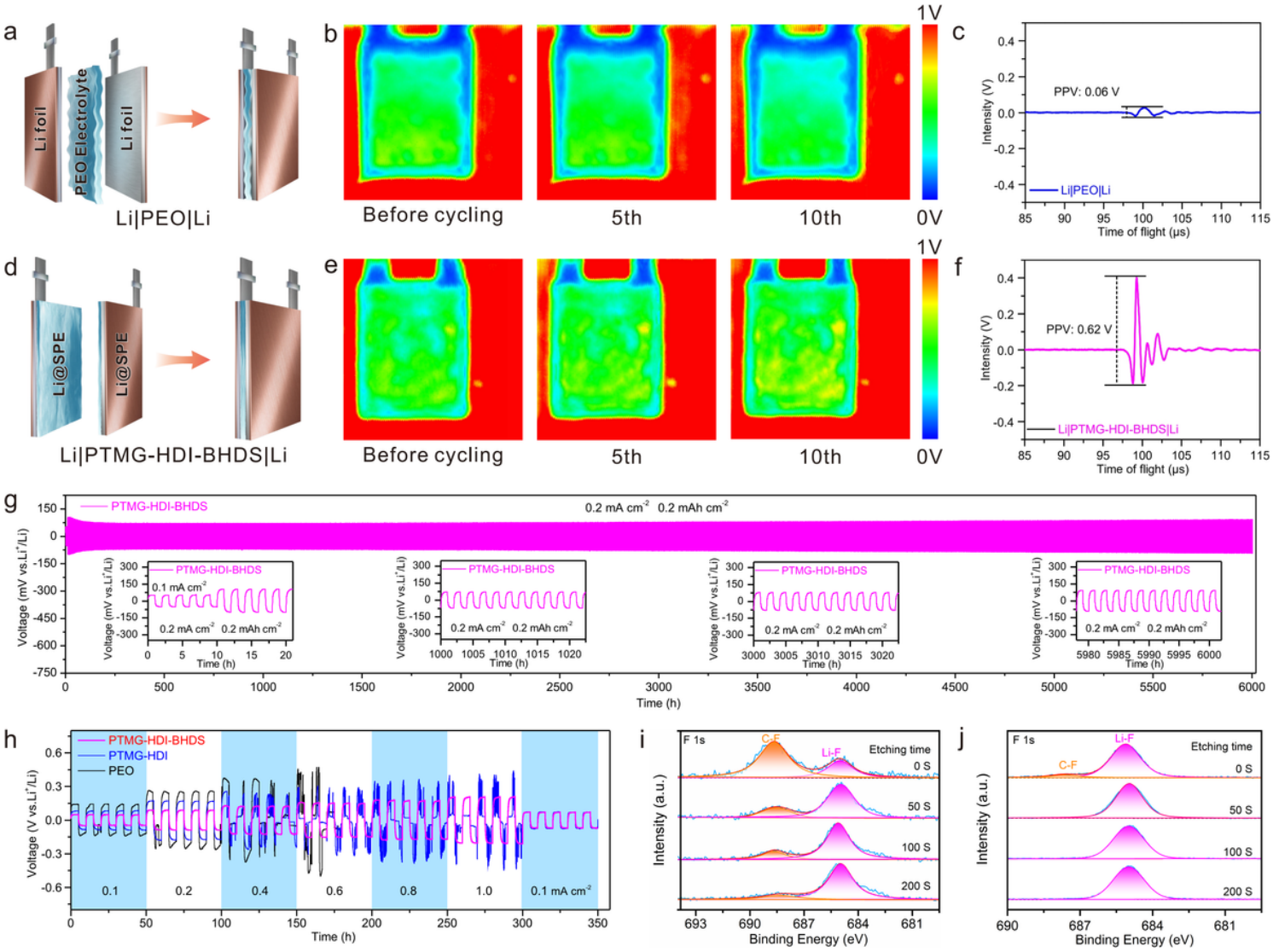

Figure 4

Electrochemical stability of the Li|SPEs|Li symmetric cells. a The internal structure of the Li|PEO|Li pouch cell. **b, c** Ultrasonic transmission images of the Li|PEO|Li pouch cell during the first 20 cycles (**b**) and the corresponding ultrasonic waves (**c**). **d** The internal structure of the Li|PTMG-HDI-BHDS|Li pouch cell. **e, f** Ultrasonic transmission images of the Li|PTMG-HDI-BHDS|Li pouch cell during the first 20 cycles (**e**) and the corresponding ultrasonic waves (**f**). **g** Galvanostatic cycling of the Li|PTMG-HDI-BHDS|Li coin cells at the current density of 0.2 mA cm^{-2}. Inset: Representative voltage profiles. **h** Rate capabilities of the Li|SPEs|Li symmetric cells. **i, j** Depth-profiled XPS of the cycled Li anodes in (**i**) Li|PEO|Li and (**j**) Li|PTMG-HDI-BHDS|Li cells.

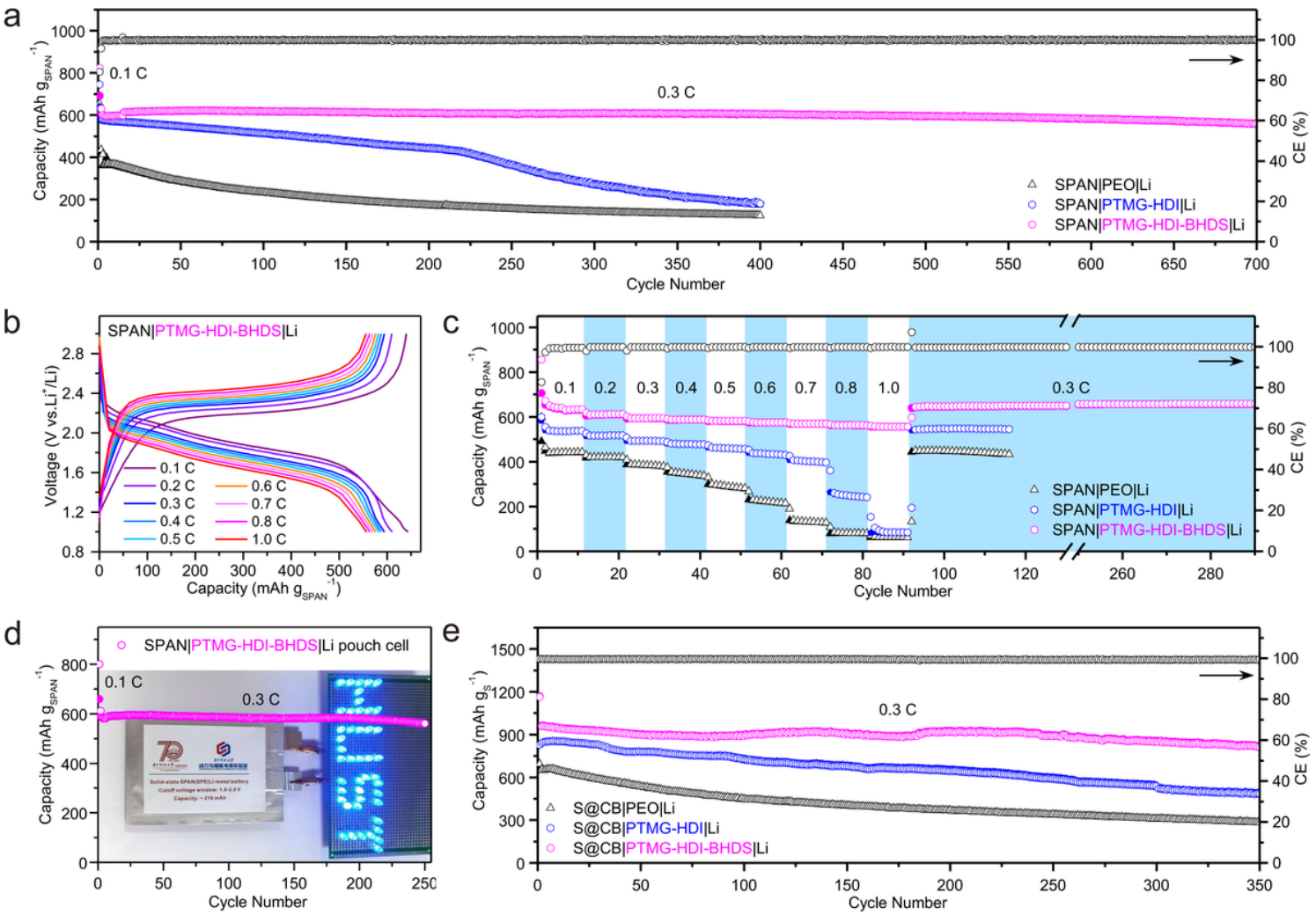

Figure 5

Electrochemical Performance of the solid-state Li-S batteries. a Long-term cycling performance of the SPAN|SPEs|Li at 0.3 C. **b** Charge/discharge curves of the SPAN|SPEs|Li cell at various rates. **c** Rate performances of SPAN|SPEs|Li cells. **d** Cycling performance and optical images (inset) of the as-fabricated SPAN|SPEs|Li pouch cell. **e** Cycling performance of the S@CB|SPEs|Li at 0.3 C. All the tests were performed at 30 ^{o}C.

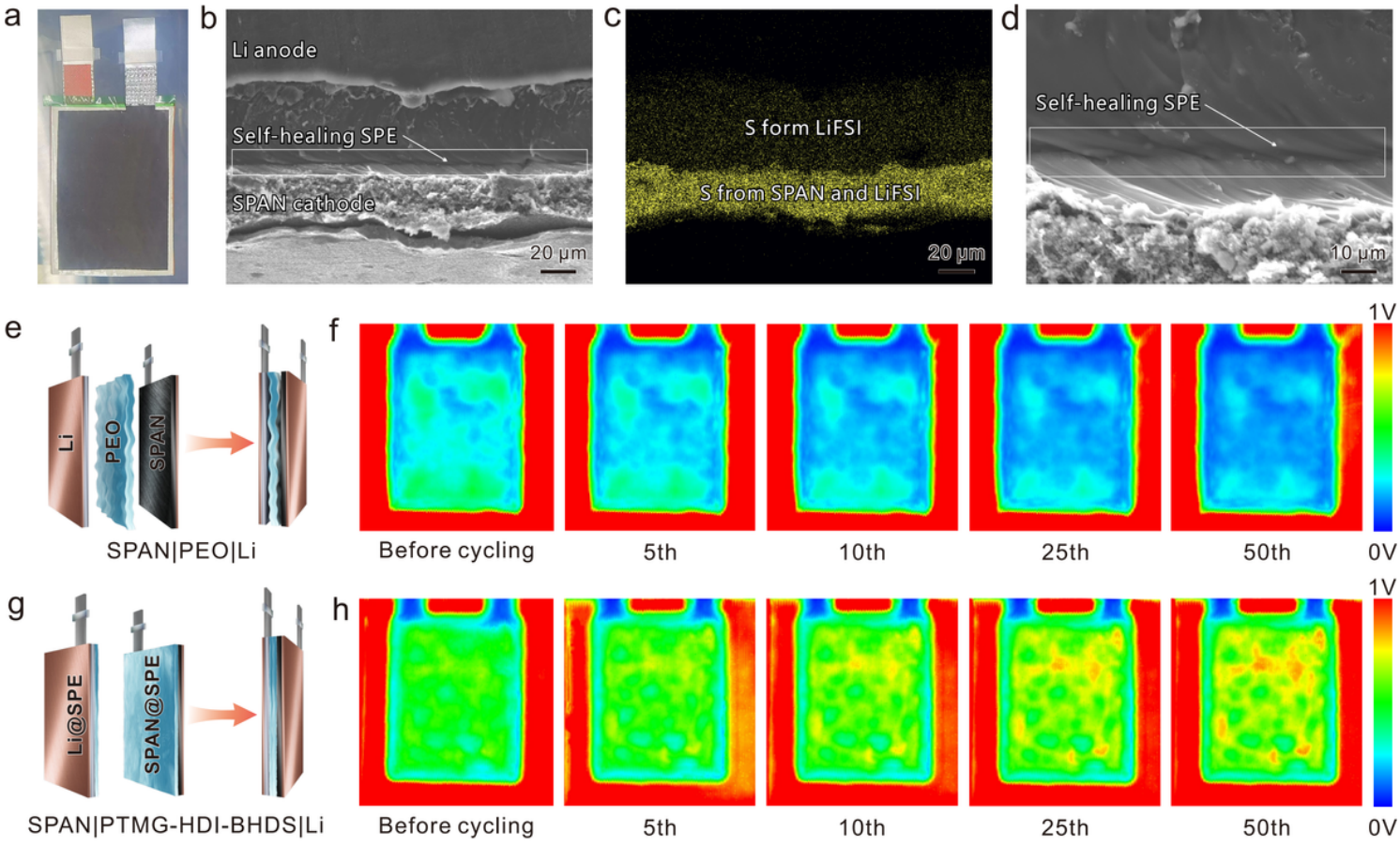

Figure 6

Stable sulfur-cathode|electrolyte|Li-anode interfaces of solid-state Li-S batteries evaluated in pouch cells. **a** Optical photographs of the integrated pouch battery. **b, c** The cross-sectional SEM image (**b**) and the corresponding EDS image (**c**) of integrated SPAN|PTMG-HDI-BHDS|Li cells. **d** The magnification SEM image of the self-healing interface. **e** The structure of the SPAN|PEO|Li pouch cell. **f**In situ ultrasonic transmission images of the SPAN|PEO|Li pouch cell during the first 50 cycles. **g** The structure of the SPAN|PTMG-HDI-BHDS|Li pouchcell. **h** In situ ultrasonic transmission images of the SPAN|PTMG-HDI-BHDS|Li pouch cell during the first 50 cycles.

Supplementary Files

This is a list of supplementary files associated with this preprint. Click to download.

- Supportinginformation.docx